Simulations of NOx Emissions from Low Emissions Discrete Jet Injector Combustor Tests

Kumud Ajmani
Vantage Partners, LLC, Cleveland, OH

Kevin Breisacher
NASA Glenn Research Center, Cleveland, OH

Abstract

An experimental and computational study was conducted to evaluate the performance and emissions characteristics of a candidate Lean Direct Injection (LDI) combustor configuration with a mix of simplex and airblast injectors. The National Combustion Code (NCC) was used to predict the experimentally measured EINOx emissions for test conditions representing low power, medium power, and high-power engine cycle conditions. Of the six cases modeled with the NCC using a reduced-kinetics finite-rate mechanism and lagrangian spray modeling, reasonable predictions of combustor exit temperature and EINOx were obtained at two high-power cycle conditions.

Introduction

The N+2 portion of NASA's Environmentally Responsible Aviation (ERA) program is exploring low NOx combustor concepts for use in aircraft gas turbine engines in the 2020 timeframe. These low emissions combustor concepts must be capable of meeting or exceeding the N+2 LTO NOx goal of a 75% reduction from the International Civil Aviation Organization (ICAO) standard adopted by the Committee on Aviation Environmental Protection (CAEP) for engine pressure ratios of 55 and higher.

In addition to the ERA combustor development efforts at engine manufacturers, a NASA Research Announcement (NRA) was used develop technologies reduce program risk. This NRA resulted in awards to three fuel injector companies to develop low emission injector concepts capable of meeting N+2 goals. The performance of these injectors was to be evaluated in NASA GRC flame tube test facilities. This paper presents results of simulations of some of the tests conducted with the United Technologies Aerospace Systems (UTAS) injector concept as part of the evaluation effort.

Hardware

Previous tests had demonstrated the ability of multipoint, small Lean Direct Injection (LDI) injectors to significantly reduce NOx emissions. However, at the operating pressures and thrust levels anticipated for N+2 engines, numerous small LDI injection points would be required. At

low power operating points, this large number of injection points would result in a low fuel flow per nozzle. Low fuel flow per nozzle would exacerbate the problem of achieving acceptable flame stability and emissions at low power conditions as had been seen in previous tests. There were also concerns that operability and manufacturability would limit the commercial potential of large arrays of small LDI injection points.

The approach taken by UTAS [1] was to explore injector diameters (~25 mm) larger than the smallest LDI injectors previously tested but comparable to other LDI concepts while altering tip geometries to enhance mixing. It was hoped that these larger diameter injectors might result in a more manageable number (a reduction by approximately a third from a previous concept [2]) of fuel injection tips for the size of engines contemplated for N+2. Over 100 nozzle configurations were examined computationally by UTAS and guided by a series of tests, which led to the geometry shown in Figure 1.which was predicted to produce acceptably low levels of NOx.

Two variations of the injector element concept are used in the test hardware. The difference in these injector elements is a slightly larger effective area, AC_d = 1.21e-4 m^2 (.1875 in^2) for the intermediate nozzles in the array compared to those of the outer nozzles which has an AC_d = 9.71e-5 m^2 (.1500 in^2). The fuel manifolding to both intermediate and outer injectors is the same. The injectors have approximately 40% of the air flowing through the highly swirling central air circuit, with the remaining air flowing through a minimally swirling outer air circuit. The fuel is delivered along a short prefilming surface which allows the inner air to circumferentially spread the fuel prior to the fuel entering the very high shear zone caused by the difference in the inner and outer swirls. The low swirling outer air circuit combined with the high swirl of the inner circuit is designed to produce an aerodynamic confinement which promotes the rapid mixing of fuel and air within a very short distance from the nozzle. Downstream of the fuel-mixing zone, the swirl from the inner air circuit dominates over the minimally swirling outer zone, retaining a high amount of overall swirl in the injector, which allows it to mix efficiently with the other injectors in the multipoint array.

The combustor concept developed utilized five rows of injectors and converging combustor wall geometry (Figure 2.). There was a single, central three-nozzle row of pilot injectors. Two rows of intermediate injectors each consisting of two nozzles and two rows of outers each consisting of three nozzles. The converging combustor walls were utilized to confine the flow and promote rapid mixing. While this combustor mixing was shown to be dependent on the angle of the outer row of injection elements through simulations, a single fixed outer row angle was used in the hardware. The combustor contour was made from a cast ceramic. The fuel to each injection element type (pilot, intermediate, and outer) was supplied by an individually controlled fuel circuit feeding a common element manifold. The range of operating conditions for the engine would be met by radially staging the rows of injectors. At low power a single row of pressure atomizing pilot injectors would be utilized to maintain flame stability [3].

Test data indicated that the measured AC_d ($2.2in^2$) for the thirteen-injector array was typically higher than the target AC_d for the array. This may have been due to air leakage around individual nozzles due to greater than anticipated thermal expansion of the hardware or due to leaking around the dome seal between the dome plate and the nozzle array. This air leakage may have led to more locally rich zones at the nozzles than was targeted. The effects of the suspected diversion of airflow are not included in the simulations below.

Tests

To evaluate the performance of this injector concept, tests were conducted in CE-5, a flame-tube combustion test facility at the NASA Glenn Research Center [4]. A schematic of the combustor section of the CE-5 flame-tube is shown on Figure 3. Nonvitiated air was used in the rig with a maximum inlet temperature of 865 K and a maximum pressure of 1380 kPa. The airflow rate was measured with a venturi meter. Jet-A was the fuel and the fuel flow rate was measured by a turbine flow meter. The combustor section downstream of the injector consists of a ceramic casting with no liner cooling. Gas probes (both stationary and traversing) were placed downstream of the injector to collect combustion products for analysis. The combusted gas samples were collected according to the standard gas-analysis procedure, SAE-ARP1256D [5]. For NO and NO2, the simultaneous chemiluminescence method was used. The rest of the combustion products were cooled down to 450 K by mixing with sprayed water before exiting to a low-pressure exhaust system.

Computational Model

The National Combustor Code (NCC) [6] was used to perform steady-state RANS simulations of the mixing and burning of a Jet-A/Air mixture. The NCC is a state-of-the-art computational tool, which is capable of solving the time-dependent, Navier-Stokes equations with chemical reactions. The NCC is being developed primarily at NASA Glenn in order to support combustion simulations for a wide range of applications, and has been extensively validated and tested for low-speed chemically reacting flows.

Second-order accurate central-differences are used for the inviscid and viscous flux discretization, and a Jameson operator (a blend of 2nd and 4th-order dissipation terms) is used to maintain numerical stability. In order to enhance convergence acceleration in pseudo-time, implicit residual smoothing is used to smooth the computed residuals. Dual time-stepping is used to obtain second-order time-accuracy for time-accurate simulations.

Turbulence closure is obtained by using a cubic, non-linear two-equation k-e model with dynamic wall-functions including pressure-gradient effects [7]. A finite-rate chemistry model is used to compute the species source-terms for Jet-A/Air chemistry. The chemistry model incorporates 13 species and 18 chemical reaction steps [8] and is detailed in Table 1.

The kinetics model uses **A** (pre-exponential factor), **n** (temperature exponent) and **E** (activation energy, cal/mol) to compute the Arrhenius rate coefficient, $\mathbf{k = A\,(T/T_0)^n\,e^{(-E/RT)}}$, for a given temperature, **T** (K). (**R** = universal gas constant, $\mathbf{T_0}$ (K) is a reference temperature). Note that reaction steps 1-3 are irreversible, and reaction steps 4-18 are formulated as reversible reactions. The kinetics for NOx prediction includes an extended Zeldovich mechanism (four steps for NO) and an additional four steps for N_2O species. The inclusion of N_2O is expected to improve the NOx predictions in the small local regions where fuel-rich burning is occurring in the flow.

National Combustion Code (NCC) Computations

The National Combustion Code (NCC) was used to perform RANS computations for six different test conditions, selected from a broad matrix of conditions tested at NASA GRC. These six conditions (see Table 2) are representative of the wide range of power conditions that would be encountered in a typical flight profile, including ground idle conditions. Some best-practices identified for computing LDI flows with the NCC [9] were used in the current computations.

The initial conditions for the NCC were those corresponding to non-reacting flow at the particular P_3 and T_3 in the entire domain. A fixed mass-flow rate and temperature was imposed at the inflow boundary, and the primary flow direction was assumed to be normal to the inflow surface. A fixed static pressure equal to P_3-Δp was imposed at the outflow boundary. The typical experimental Δp (as measured by a difference of P_3 and P_4) for all cases computed with the NCC was for a 3% pressure drop across the injector array.

A typical NCC computation proceeds from an initial solution as follows:

1. Run non-reacting flow until steady-state convergence (<0.1% difference in mass-flow rate between inflow and outflow boundary over 500 consecutive iterations) is achieved.
2. Introduce fuel flow at fuel inlets in the form of liquid spray particles. The initial injection location, injection velocity, particle size (SMD) and initial temperature of the liquid fuel for all the injectors were provided by UTAS. The NCC lagrangian spray solver [10] modeled the pilot elements as a hollow spray (60^o cone angle, 10^o cone thickness) with 32 streams and 10 droplet groups. Each intermediate and outer element was modeled as a ring of 16 discrete holes distributed along the outer circumference of the nozzle to mimic the annular film injection of each airblast element. Each discrete hole was modeled as a solid cone spray (10^o cone angle) with 4 streams and 8 droplet groups.
3. Introduce a "spark" source-term, in a small volume downstream of each injector, for 1000 iterations, or until the temperature in each cell of the "spark" zone reaches 1600K, whichever is earlier. Reacting-flow, with finite-rate chemical kinetics (see Table 1) is initiated in this step.
4. Run reacting-flow computations (RANS) until steady state convergence (exit plane mass-averaged temperature and EINOx are within 1% variation over 1000 successive iterations) is achieved.

Computational Results (NCC RANS)

Figure 4 shows the computational geometry, and several cross-sectional slices of the fully tetrahedral mesh generated for the thirteen-element LDI injector. The three pilot elements, the four intermediate elements and the six outer elements were each meshed with particular attention being given to the entrance region, the injector passages and the exit region of each element. In addition, the main mixing region in the combustor, immediately downstream of the injector elements, was also refined.

Several progressively finer mesh refinements were attempted to meet "effective area" prediction criteria. The refinement was considered "converged" when a non-reacting flow computation with a given mesh provided an "acceptable" effective area as compared to the experimental effective area (A_{cd}) measurement. The predicted effective area was computed from the NCC predicted pressure drop for a given airflow rate and air density. All the computational results presented here were obtained with a final mesh consisting of 12M tetrahedral elements. The predicted AC_d for the NCC computations was 15%-20% higher than the experimental effective area of 2.2 in^2.

Figures 5-16 show computed contours at five different cross-sections each, for each of the six conditions listed in Table 2. The final two columns of Table 2 list the NCC predictions of 'exit' plane gas-temperature (T_4) and EINOx. The reported T_4 and EINOx for the NCC code were obtained by performing a mass-weighted average of the quantities at each computational element in the 'exit' plane. This 'exit' plane is located at the end of the converging section of the combustor. The best comparison between NCC and experimental data is obtained for the "high power" cases RDG 169 and RDG 192 (P_3=250psi). For both cases, the NCC prediction of T_4 and EINOx is within 5% and 10% of the experimental measurements, respectively.

Low Power – Pilots Only

Figure 5 shows the temperature contours for the RDG011 case that represents a typical *low-power* configuration. The three pilot elements are fueled (local FAR=0.164, ϕ=2.4), while the remaining (intermediate and outer) elements flow air only (global FAR=0.0161, ϕ=0.2367). The disparity in the high temperature local stream downstream of the pilots and the surrounding low temperature stream (air only) results in relatively poor mixing, as can be seen in Figure 5(a) (pilot element and two outers) and 5(b) (intermediate element). The NCC predicts a T_4 temperature of 1255K at the 'exit' plane, as compared to an 'equilibrium', well-mixed T_4 of 1138K as computed by the CEA code [7]. As seen in Figure 5(e), the computed flow is far from being in a fully mixed state at the 'exit', and the NCC tends to over-predict the T_4 for these poorly mixed conditions with very high local equivalence ratios downstream of the pilots.

The contour plots in Figure 6 show the NOx mass-fraction distribution for the RDG011 case at different cross-sections of the combustor. The NCC prediction of EINOx=13.1 and EICO=1.11 is extremely poor, when compared to the experimental measurements of 4.9 and 26.0, respectively. The poor prediction by NCC RANS for poorly-mixed flows with very rich (> 2.0)

local equivalence ratios is an area that can be improved by use of turbulence-chemistry interaction modeling, optimized kinetics for high equivalence ratios and improved spray modeling based on better diagnostics for sprays in low-power conditions.

Intermediate Power – Effect of Varying Fuel-Splits

Figures 7-12 show temperature and NO mass-fraction contours for three *intermediate-power* cases with varying fuel-splits for the three types of injector elements. The RDG094 case corresponds to a 13.3%/86.7% fuel split (local FAR=0.029/0.056, ϕ=0.43/0.82) between the pilots and intermediates, with the outers turned off (global FAR=0.0207, ϕ=0.3044). The contour plots in Figure 7 and 8 show the computed temperature and NOx mass-fraction distributions at different cross-sections for the RDG094 case. The NCC prediction of T_4=1499K was only in ~3% error as compared to the CEA computed T_4=1540K (based on T_3=658K, ϕ=0.3044). The temperature contours in figures 7(a) and 7(b) show considerably better mixing, particularly between the pilots and intermediates, than the low-power case (pilots only, RDG011) discussed earlier. The NCC prediction of T_4 thus matches the 'well-mixed' equilibrium values computed from the CEA code. However, the NCC prediction of EINOx=22.1 is 144% higher than the experimentally measured value of 9.06, which follows the over-prediction trend for the RDG011 (poorly mixed) case. Note that no significant CO was measured at the exit plane for this case, because of the very high combustion efficiency (> 99%). The NOx production downstream of the pilots is higher than the intermediates (see figure 8), even though the local FAR for the pilots is almost half of that of the intermediates. This is perhaps because the simplex nozzles (used in the pilots) tend to generate more NOx than airblast nozzles (used in the intermediates) – a phenomenon also noted in the computational and experimental work reported by Ajmani [8].

A second *intermediate power* case (RDG 100) with a 27%/63% fuel-split (local FAR=0.059/0.047, ϕ=0.867/0.692) between the pilots/intermediates, with outers turned off (global FAR=0.0259, ϕ=0.381) was computed to study the effect of varying the fuel split between the pilots and intermediates. This case also had a 25% higher global fuel-air ratio than the previous RDG094 case. The NCC prediction of T_4=1538K was in ~7% error as compared to the CEA computed T_4=1648K (based on T_3=655K, ϕ=0.381). The temperature contours are shown in figure 9, and the change in fuel-split improves the mixing between the pilots and intermediates (see figure 9(e)) due to the reduction in disparity between their respective local FAR, as compared to the previous RDG094 case. The NCC predicts an EINOx value of 20.85, as compared to the experimental measurement of 13.3, which is an improvement of the over 100% error in EINOx prediction for RDG011 and RDG094. Figure 10 shows that the pilots contribute much more to NOx production than the intermediates (see figure 10(a), 10(c)), because of their near-stoichiometric *local* fuel-air ratios.

Figures 11 and 12 show computed contours for a third *intermediate power* case (RDG 111) with a 16%/43%/41% fuel-split between the pilots, intermediates and outer elements (local

FAR=.034/.028/.022, ϕ=0.50/0.41/0.32) for a global FAR=0.0207 (ϕ=0.3044). The NCC prediction of T_4=1584K was in ~3% error as compared to the CEA computed T_4=1540K (based on T_3=654K, ϕ=0.3044). The temperature contours in figure 11 show that the flow downstream of the pilots has the highest temperature among the three types of injector element, and the flow is fairly well mixed at the exit plane location (figure 11e).

A relatively high experimental EICO of 14.2 was recorded for this case (RDG111), indicating relatively low combustion efficiency (as compared to RDG 094 and RDG100). The recorded EINOx of 1.5 was the lowest among the six cases studied in this paper. The NCC predictions for EICO (1.5) and EINOx (15.0) were poor, as compared to the experimental data. As seen before in the low power, low combustion efficiency case (RDG 011), the intermediate-power, low combustion efficiency case also represents a challenge for the NCC code. The NCC predicts that the pilot elements dominate the NOx production among all of the elements (figure 12). This case is another candidate for further analysis with turbulence-chemistry interaction modeling and/or Time-Filtered Navier-Stokes (TFNS) with the NCC.

High Power – Effect of Varying T3

The final two experimental configurations computed with the NCC (RDG 169 and RDG 192 in Table 2) represent *high power* conditions for the combustor. Figures 13 and 14 show computed contours of temperature and EINOx for RDG 169 with a 9%/35%/56% fuel-split (local FAR=.02/.036/.028, ϕ=0.29/0.53/0.41) and a global FAR=0.0285 (ϕ=0.42) at P_3=1.73MPa (250psi), T_3=817K (1011F) and combustion efficiency greater than 99.5%. The hot flow from the various elements is very well mixed at the exit plane, compared to the low-power and intermediate-power cases (figure 13e). The NCC prediction of T_4=1538K is in ~9% error as compared to CEA's 'equilibrium' value of T_4=1648K. The maximum amount of NOx is produced downstream of the pilot elements, followed by the outers, and the intermediates (see figure 14). The NCC prediction for EINOx (mass weighted area average at exit plane) is 9.2, which compares very well with the measured value of 8.3. This indicates that the RANS NCC approach works well for flows that are relatively well mixed out and have high combustion efficiency.

The second *high power* condition (RDG 192) had an experimental fuel-split of 8%/35%/57% (local FAR=.035 / .033 / .035, ϕ=0.515/0.485/0.515) for a global FAR=0.03 (ϕ=0.44) at P_3=1.73MPa (250psi), T_3=930K (1214F) and combustion efficiency greater than 99.5%. These conditions represent an even FAR for all the elements, and a 14% higher T_3 as compared to RDG 169. Several high temperature "hot spots" are predicted downstream of the pilot elements (figure 15a, 15b), and some of these "hot spots" persist downstream to the exit plane (figure 15e). The NCC prediction of T_4=1727K is in ~9% error (similar to RDG 169) as compared to CEA's 'equilibrium' value of T_4=1813K. Figure 16 shows that NOx production is dominated by the pilot elements (see figure 16c) and several local peaks of NOx are seen at the exit plane (figure 16e). The RDG 192 case has 75% higher local FAR (0.035) for the pilot elements, as compared

to RDG 169 (0.02), and this contributes to the much higher NOx production behind the pilots. The NCC prediction for EINOx (mass weighted area average at exit plane) is 9.7, which is only 11% lower than the measured value of 10.9. Hence, despite the local peaks in T_4 and NOx at the exit plane, the NCC RANS predictions for this high power, high combustion efficiency case compare well with the experimental data.

Figures 17 and 18 show a comparison of NCC predictions and experimental *traverse* probe data of EINOx measurements for the two high power cases (RDG 169 and RDG 192) summarized above. The *traverse* probe measured EINOx values at five discrete locations at the centerline (perpendicular to the longer side) of the rectangular exit plane. The NCC predictions for RDG 169 (figure 17) are qualitatively better than those for RDG 192 (figure 18), particularly at the span wise location between y=-0.5in and y=0.5in, where the experimental measurements may not have been influenced by wall effects.

In order to gain further insight into the structure of the combusting flow predicted by the NCC, two sets of iso-surfaces of temperature were plotted for the RDG 192 case. Figures 19 and 20 show *multiple*-valued and *single*-valued (1800K) iso-surfaces of temperature, indicating the degree of mixing and interactions between temperature fields produced by the pilots, the intermediates and the outer rows of injectors. A distinct lack of mixedness is seen between the flow streams downstream of the 'hotter' pilots (red) and the 'colder' intermediates (blue) in the first half of the combustor, with some mixedness being recovered in the second half due to the converging outer walls of the combustor.

Conclusions

A successful experimental and computational study was conducted to evaluate the performance and emissions characteristics of a candidate Lean Direct Injection (LDI) combustor configuration to meet NASA N+2 technology goals. The National Combustion Code (NCC) performed reasonably well in predicting the experimentally measured EINOx emissions for well-mixed, high-power engine cycle conditions. The NCC predictions for engine cycle conditions representing low/medium power and/or relatively poorly mixed flows could use significant improvement. These improvements could possibly be achieved by using computational methods like Time-Filtered Navier Stokes (TFNS) and turbulence-chemistry interaction modeling. These two methods were available in the NCC, but were not used here because of the relatively fast turnaround time required to support the experimental analysis in this study. Improvements in spray modeling and kinetics modeling, based on better diagnostic data for high-pressure and high-temperature cycle conditions, could further enhance the predictive capabilities of the current CFD approaches detailed in this paper.

Tables and Figures

	Reaction	A	n	E
1	C11H21 + O2 => 11CH + 10H + O2	1.00E+12	0.00	3.00E+04
	GLO / C11H21 0.8/			
	GLO / O2 0.8/			
2	CH + O2 => CO + OH	2.00E+15	0.00	3.00E+03
3	CH + O => CO + H	3.00E+12	1.00	0.00E+00
4	H2 + O2 <=> H2O + O	3.98E+11	1.00	4.80E+04
5	H2 + O <=> H + OH	3.00E+14	0.00	6.00E+03
6	H + O2 <=> O + OH	4.00E+14	0.00	1.80E+04
7	H2O + O2 <=> 2O + H2O	3.17E+12	2.00	1.12E+05
8	CO + OH <=> CO2 + H	5.51E+07	1.27	-7.58E+02
9	CO + H2O <=> CO2 + H2	5.50E+04	1.28	-1.00E+03
10	CO + H2 + O2 <=> CO2 + H2O	1.60E+14	1.60	1.80E+04
11	N + NO <=> N2 + O	3.00E+12	0.30	0.00E+00
12	N + O2 <=> NO + O	6.40E+09	1.00	3.17E+03
13	N + OH <=> NO + H	6.30E+11	0.50	0.00E+00
14	N + N + M <=> N2 + M	2.80E+17	-0.75	0.00E+00
15	H + N2O <=> N2 + OH	3.50E+14	0.00	7.55E+02
16	N2 + O2 + O <=> N2O + O2	1.00E+15	0.00	3.02E+02
17	N2O + O <=> 2NO	1.50E+15	0.00	3.90E+04
18	N2O + M <=> N2 + O + M	1.16E+15	0.00	3.32E+04

14 SPECIES: C11H21 CH O2 CO H2O N2 O N NO OH H H2 CO2 N2O

Table 1. Kinetics mechanism for Jet-A fuel surrogate

Case	P3 (MPa)	T3 (K)	FUEL SPLIT Pilot/Inter/Outer	FAR SPLIT Pilot/Inter/Outer	T4 (K) (CEA)	FAR (Total)	EINOx (Expt)	T4 (K) (NCC)	EINOx (NCC)
RDG 011	0.56	538	1.0 / 0 / 0	.164 / 0 / 0	1138	0.0161	4.90	1255	13.10
RDG 094	1.413	658	.133 / .867 / 0	.029 / .056 / 0	1540	0.0207	9.06	1499	22.10
RDG 100	1.434	655	.269 / .731 / 0	.059 / .047 / 0	1648	0.0259	13.29	1538	20.85
RDG 111	1.372	654.4	.16 / .43 / .41	.034 / .028 / .022	1540	0.0207	1.25	1584	15.00
RDG 169	1.730	816.7	.095 / .348 / .557	.020 / .036 / .028	1800	0.0285	8.28	1696	9.17
RDG 192	1.729	930	.081 / .353 / .566	.035 / .033 / .035	1813	0.0300	10.94	1727	9.70

Table 2. Summary of Experimental Cases Modeled with NCC

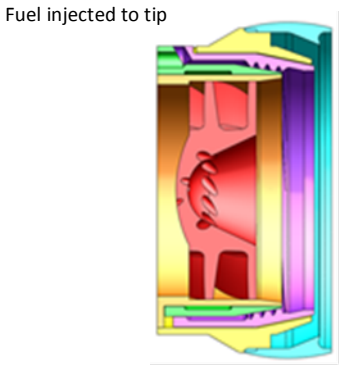

Figure 1. – Cross-section of pilot.

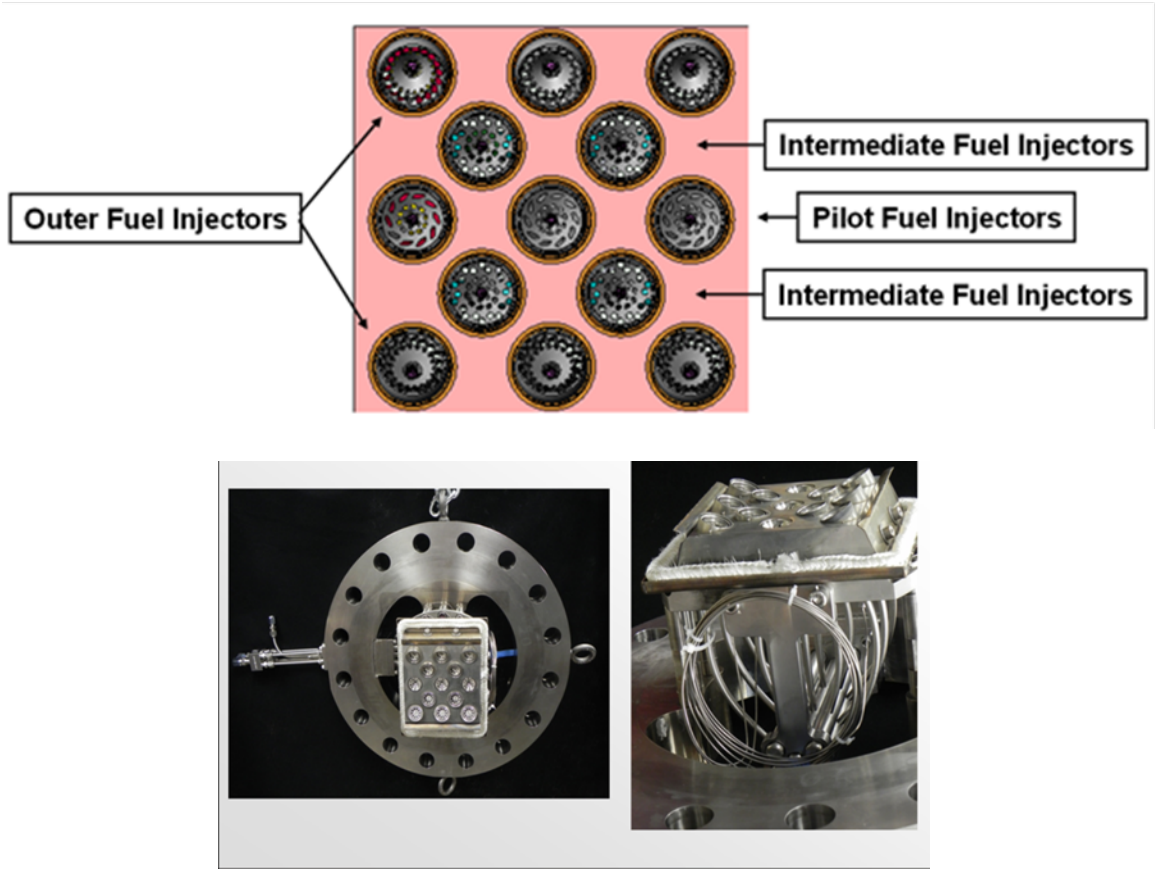

Figure 2. – Layout of injector face showing outer, intermediate, and pilot nozzles and injector hardware.

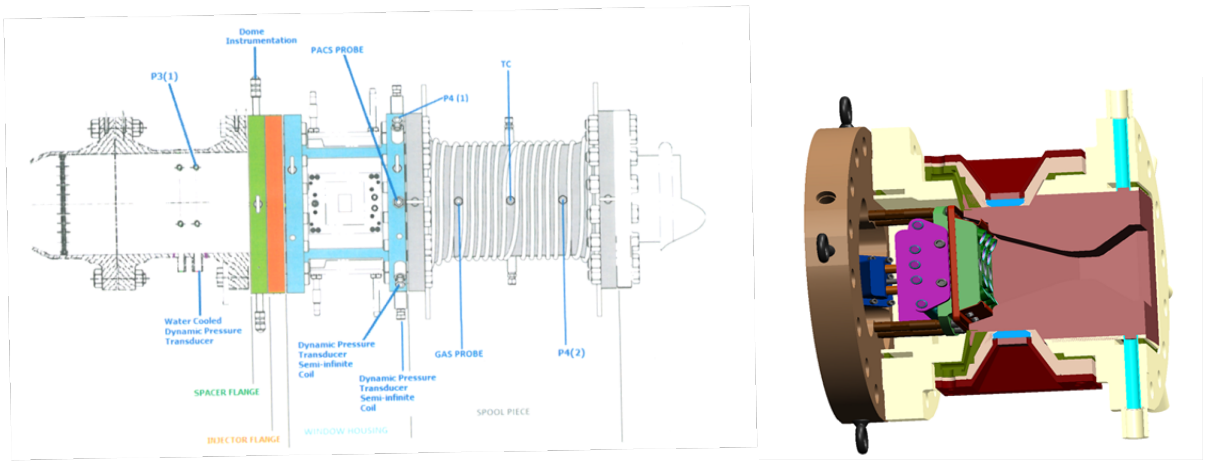

Figure 3. – Schematic of CE-5 flame tube combustor section with instrumentation locations (all dimensions in inches) and installed injector with ceramic combustor liner (right).

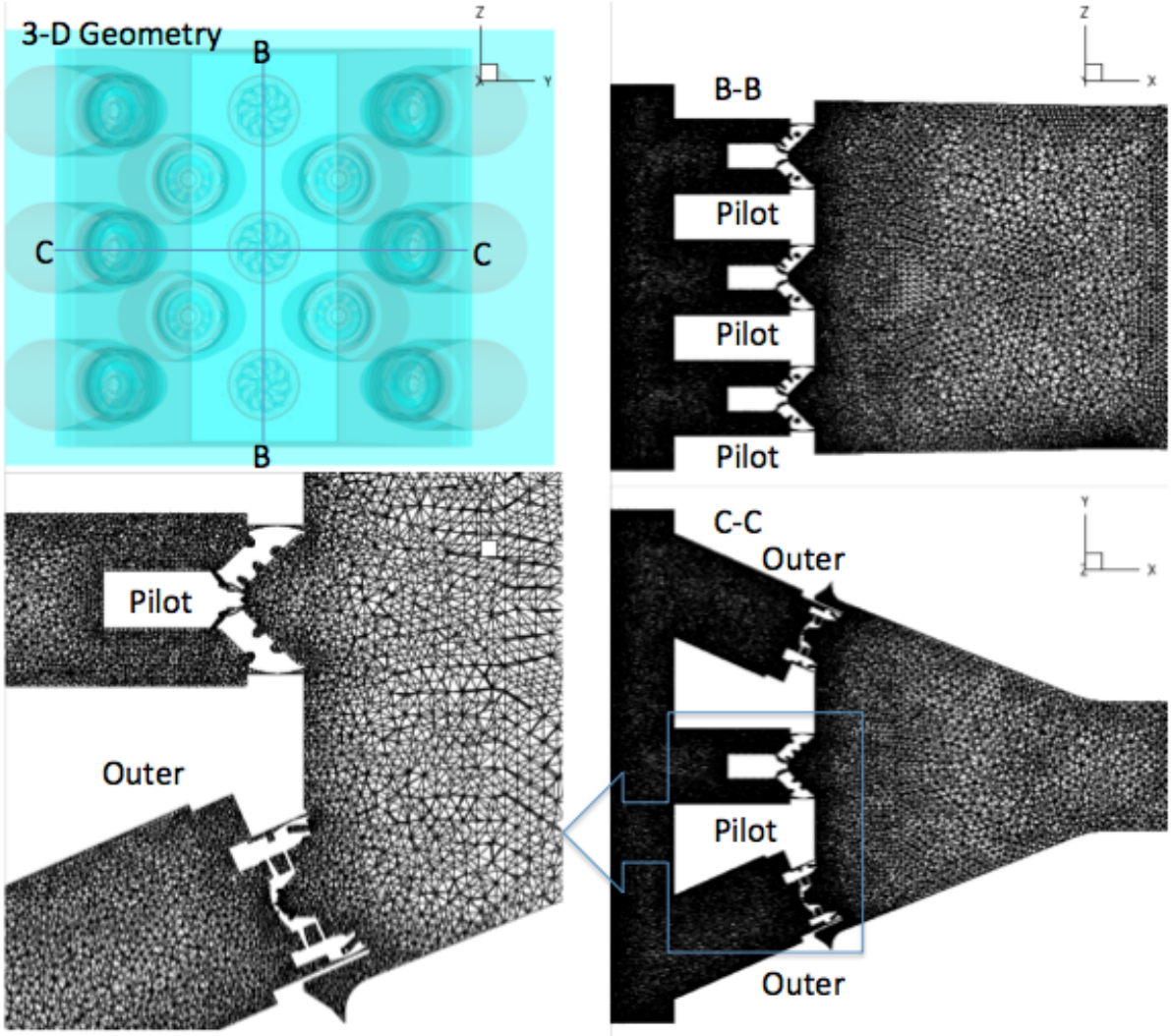

Figure 4 – Geometry and mesh at various cross-sections for CFD

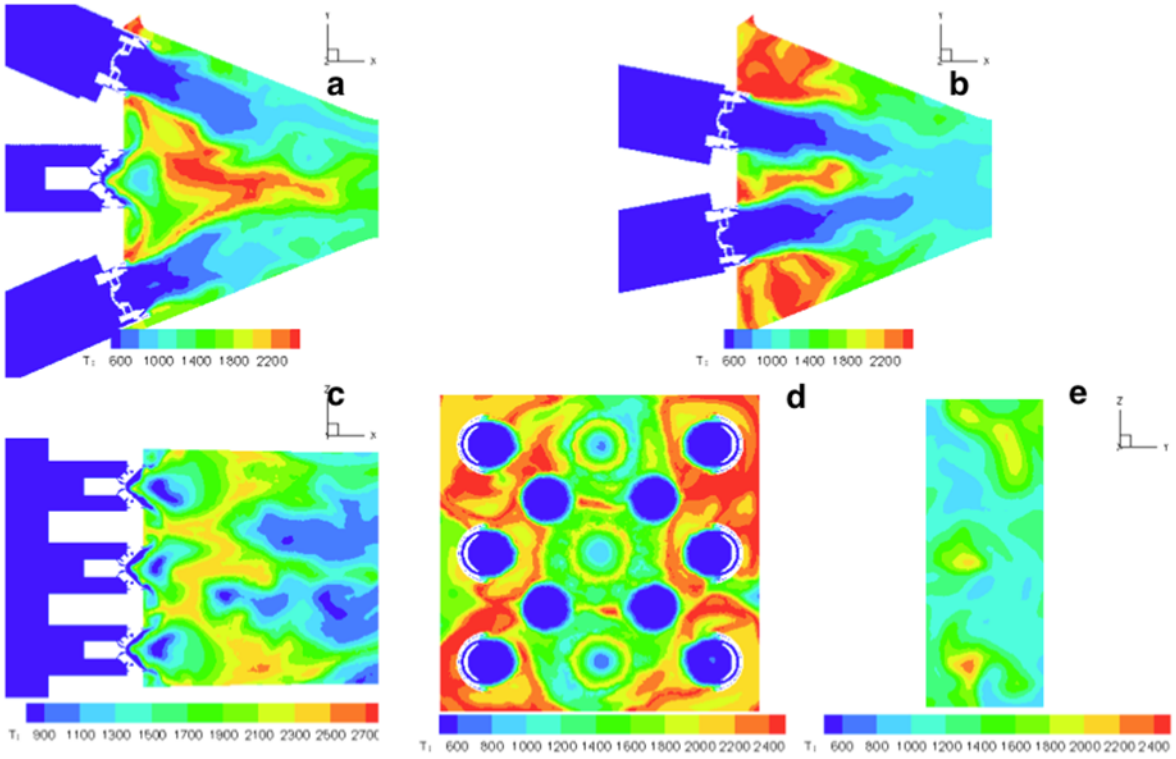

Figure 5 RDG011 – Temperature (K) Contours (a) outers, pilot (b) intermediates (c) pilots (d) face (e) exit

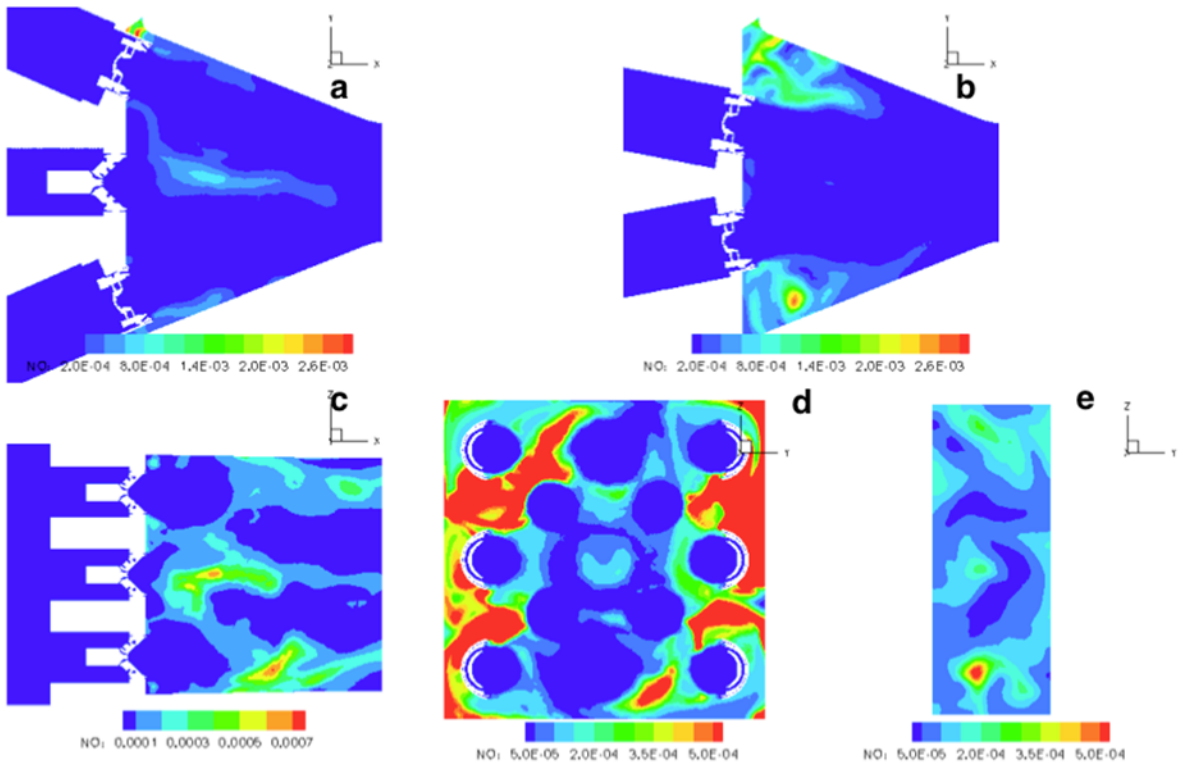

Figure 6 RDG011 – NOx mass-fraction contours (a) outers, pilot (b) intermediates (c) pilots (d) face (e) exit

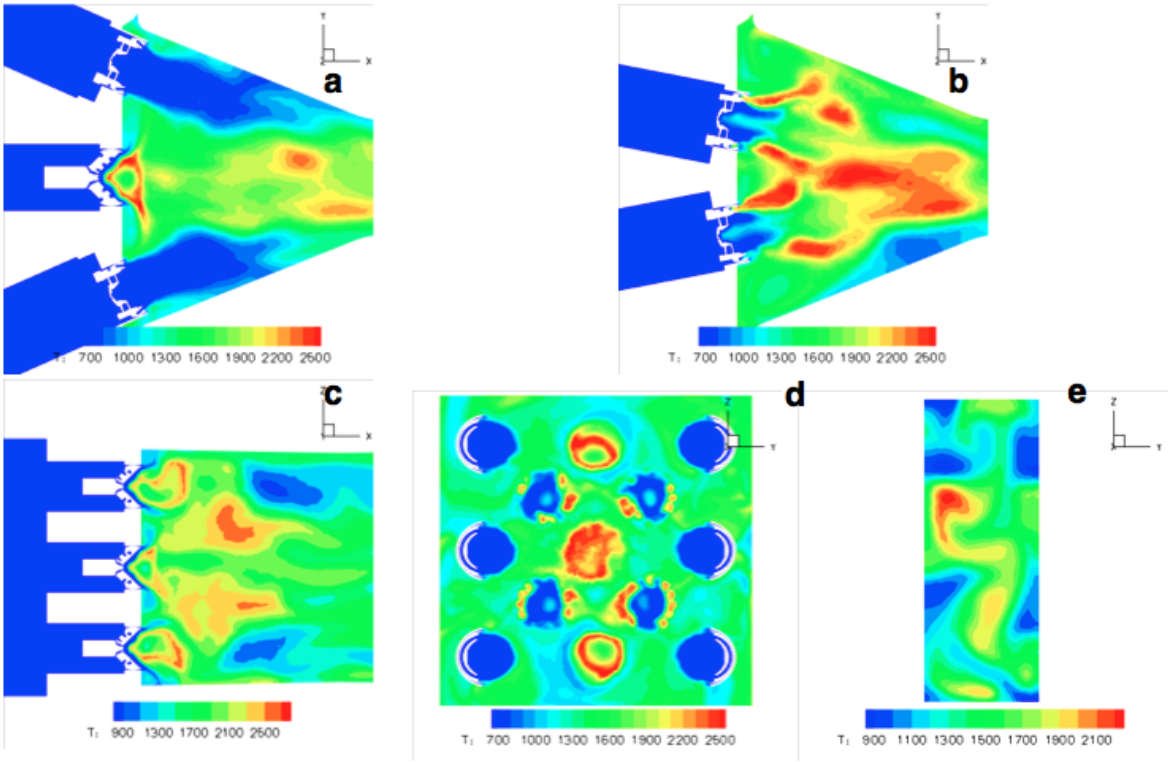

Figure 7 RDG094 – Temperature (K) Contours (a) outers, pilot (b) intermediates (c) pilots (d) face (e) exit

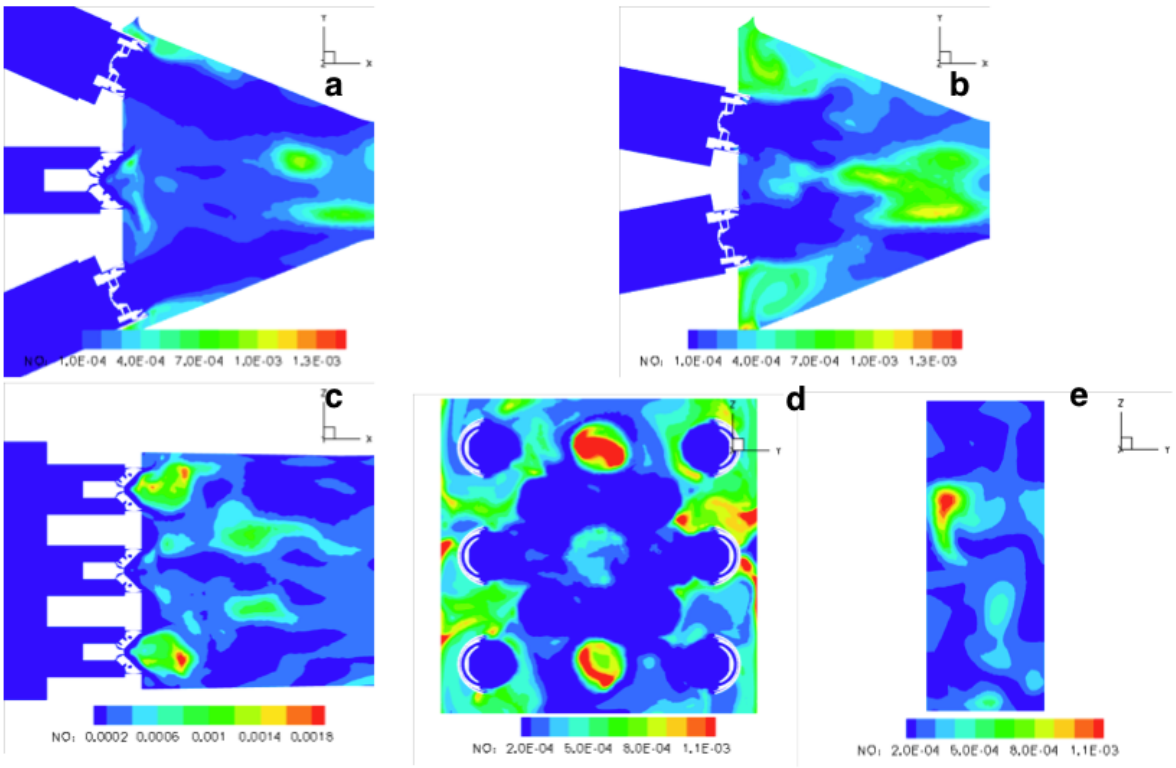

Figure 8 RDG094 – NOx mass-fraction contours (a) outers, pilot (b) intermediates (c) pilots (d) face (e) exit

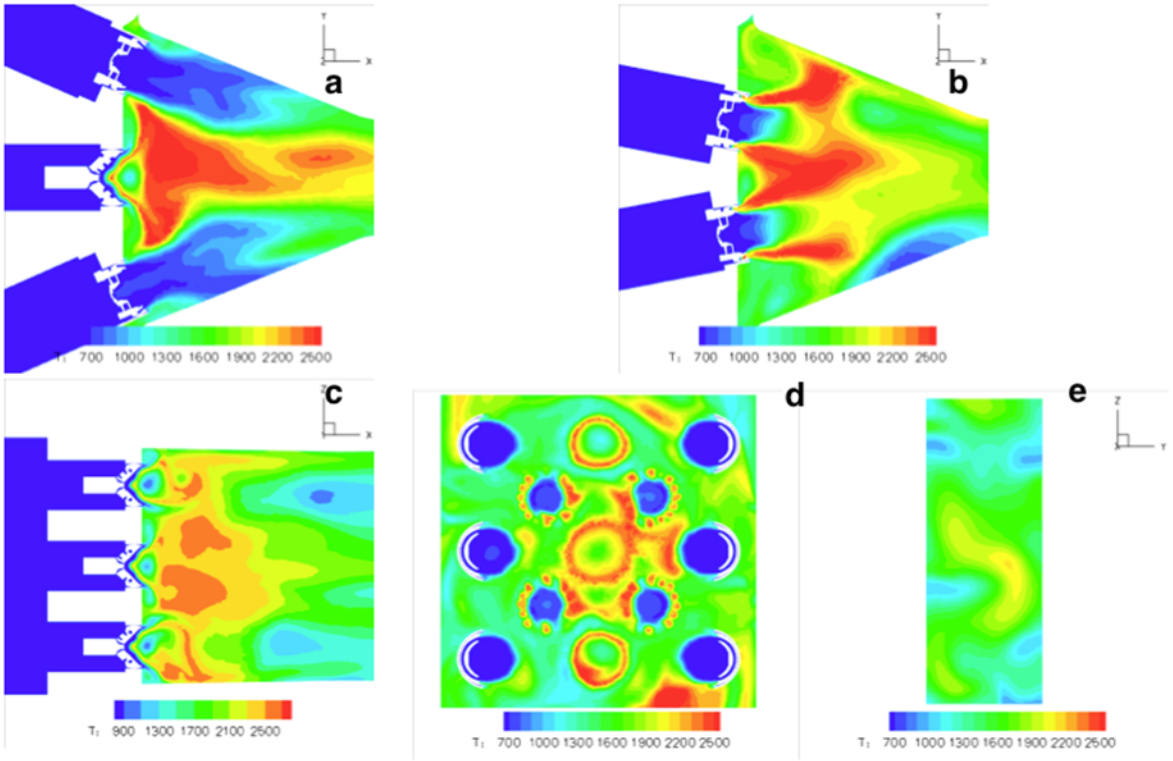

Figure 9 RDG100 – Temperature (K) Contours (a) outers, pilot (b) intermediates (c) pilots (d) face (e) exit

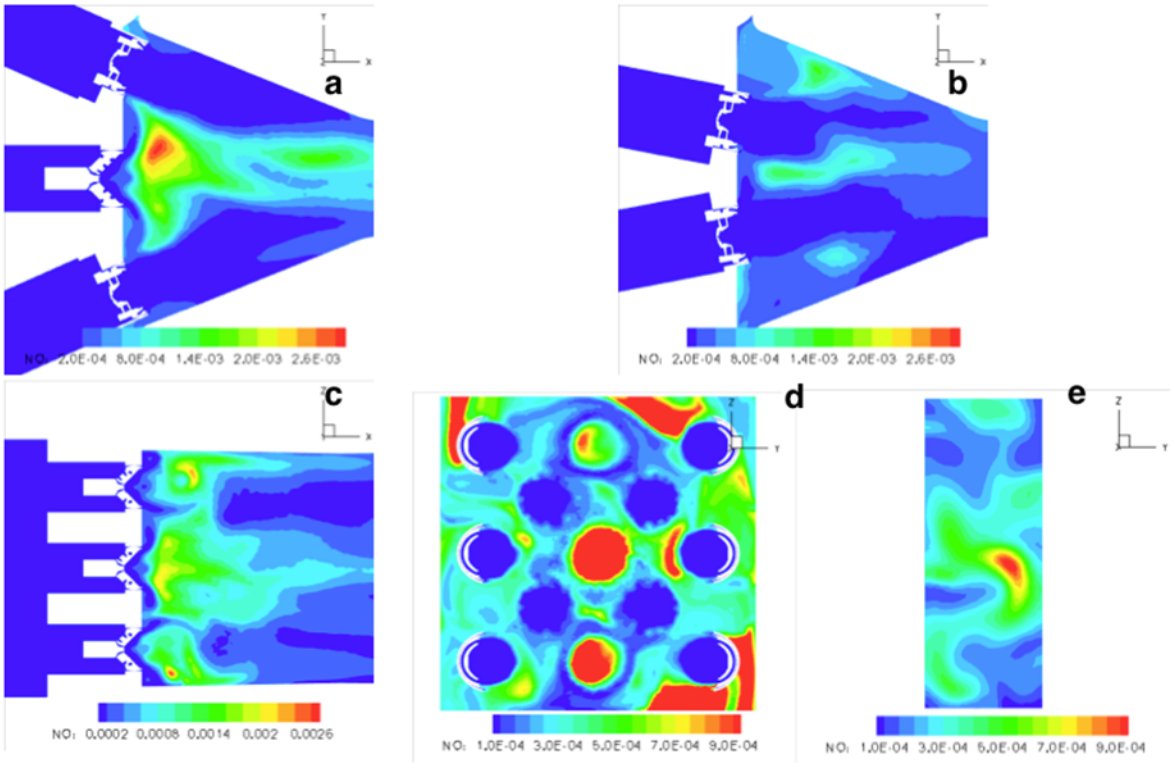

Figure 10 RDG100 – NOx mass-fraction contours (a) outers, pilot (b) intermediates (c) pilots (d) face (e) exit

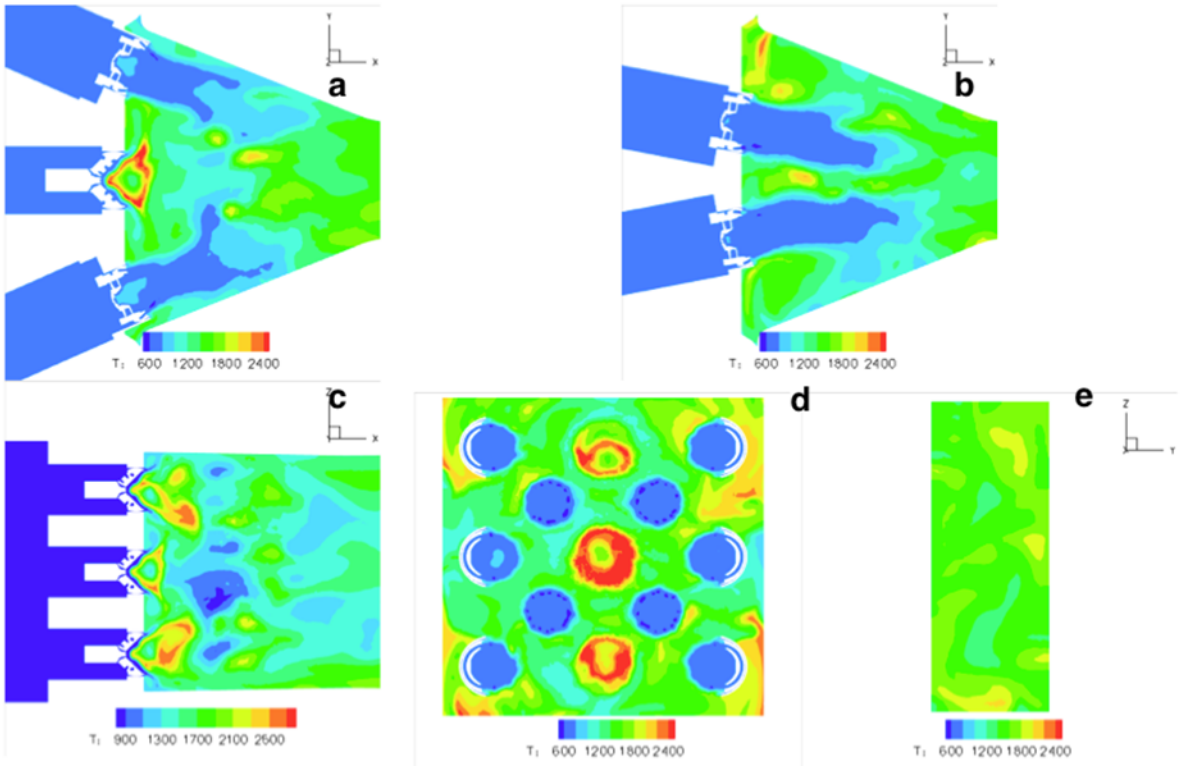

Figure 11 RDG111 – Temperature (K) Contours (a) outers, pilot (b) intermediates (c) pilots (d) face (e) exit

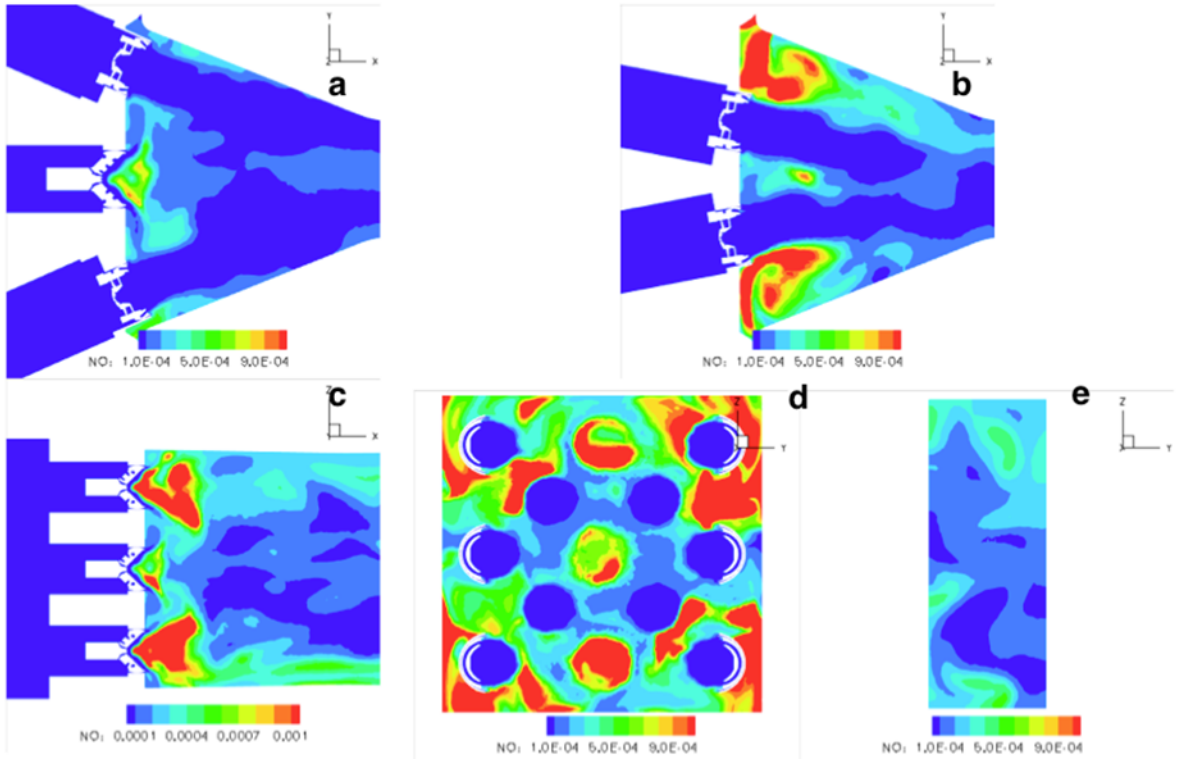

Figure 12 RDG111 – NOx mass-fraction contours (a) outers, pilot (b) intermediates (c) pilots (d) face (e) exit

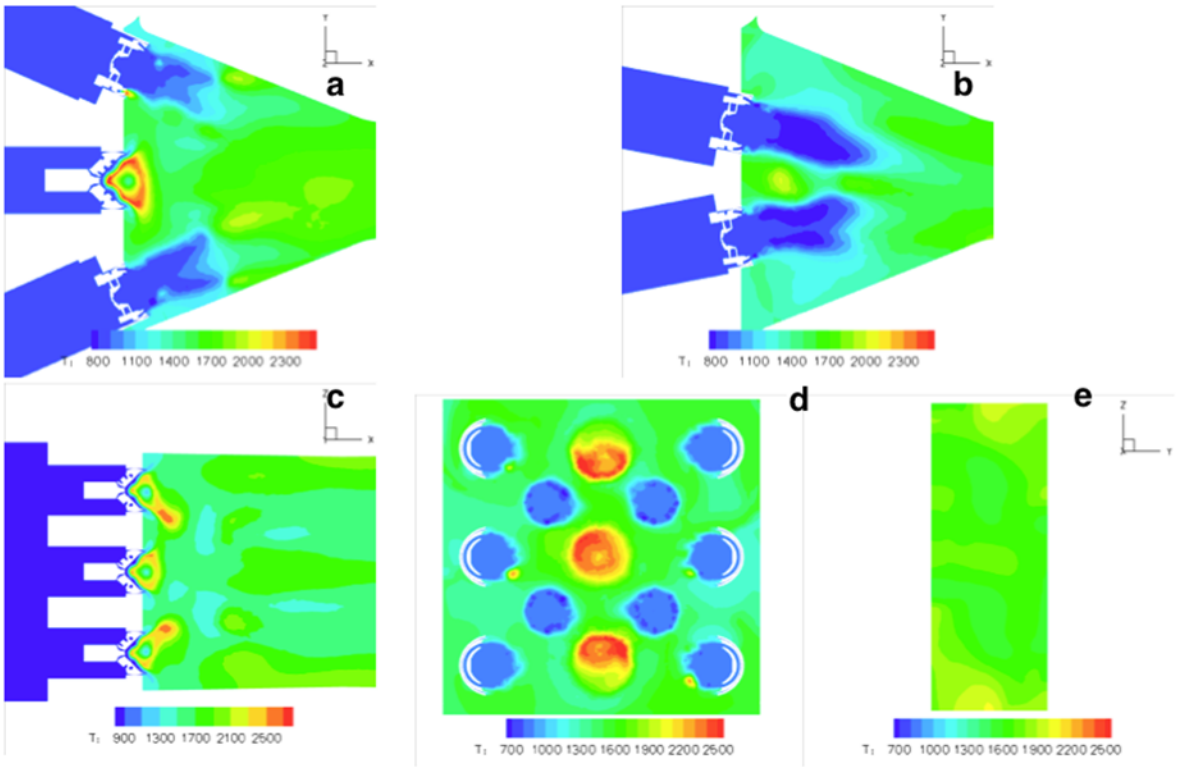

Figure 13 RDG169 – Temperature (K) Contours (a) outers, pilot (b) intermediates (c) pilots (d) face (e) exit

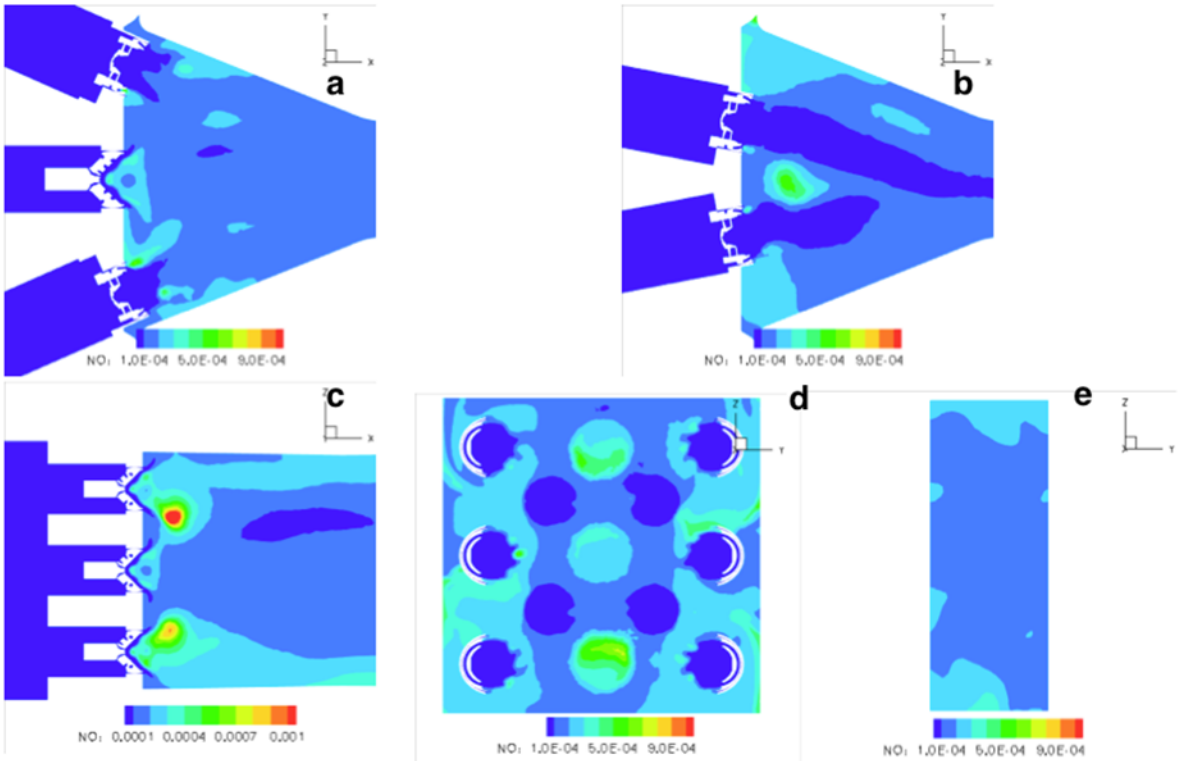

Figure 14 RDG169 – NOx mass-fraction contours (a) outers, pilot (b) intermediates (c) pilots (d) face (e) exit

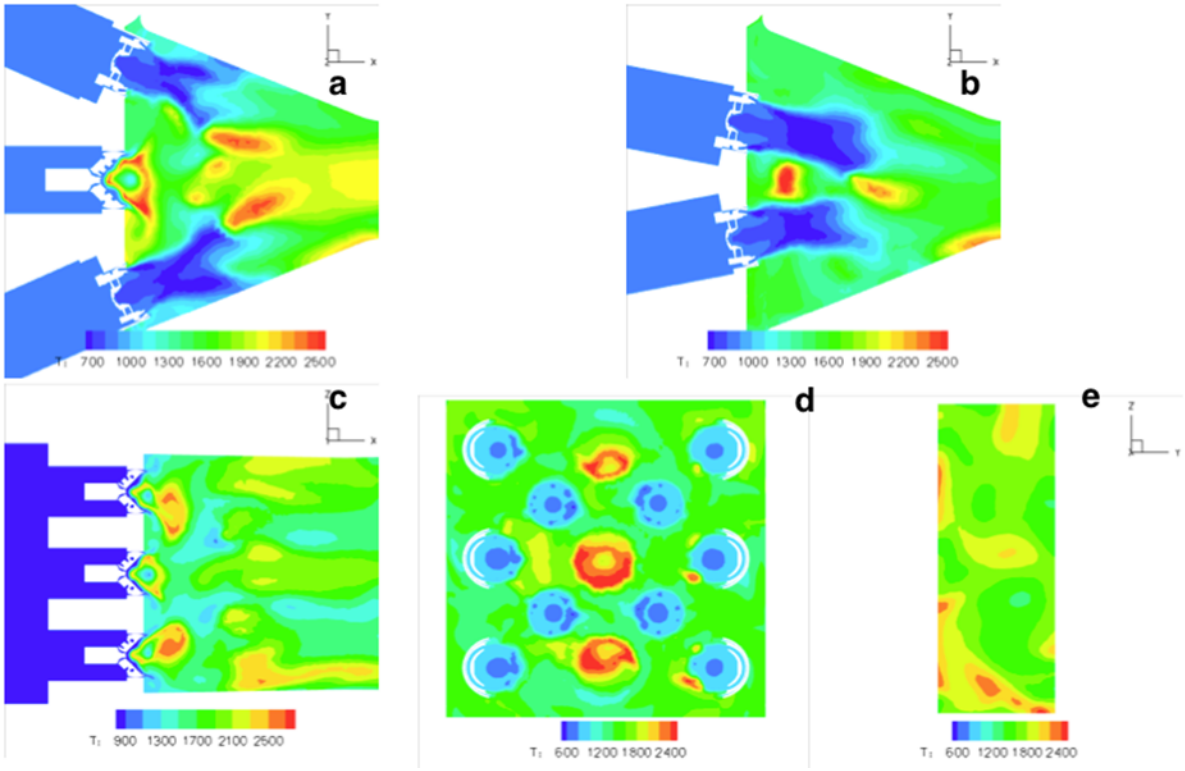

Figure 15 RDG192 – Temperature (K) Contours (a) outers, pilot (b) intermediates (c) pilots (d) face (e) exit

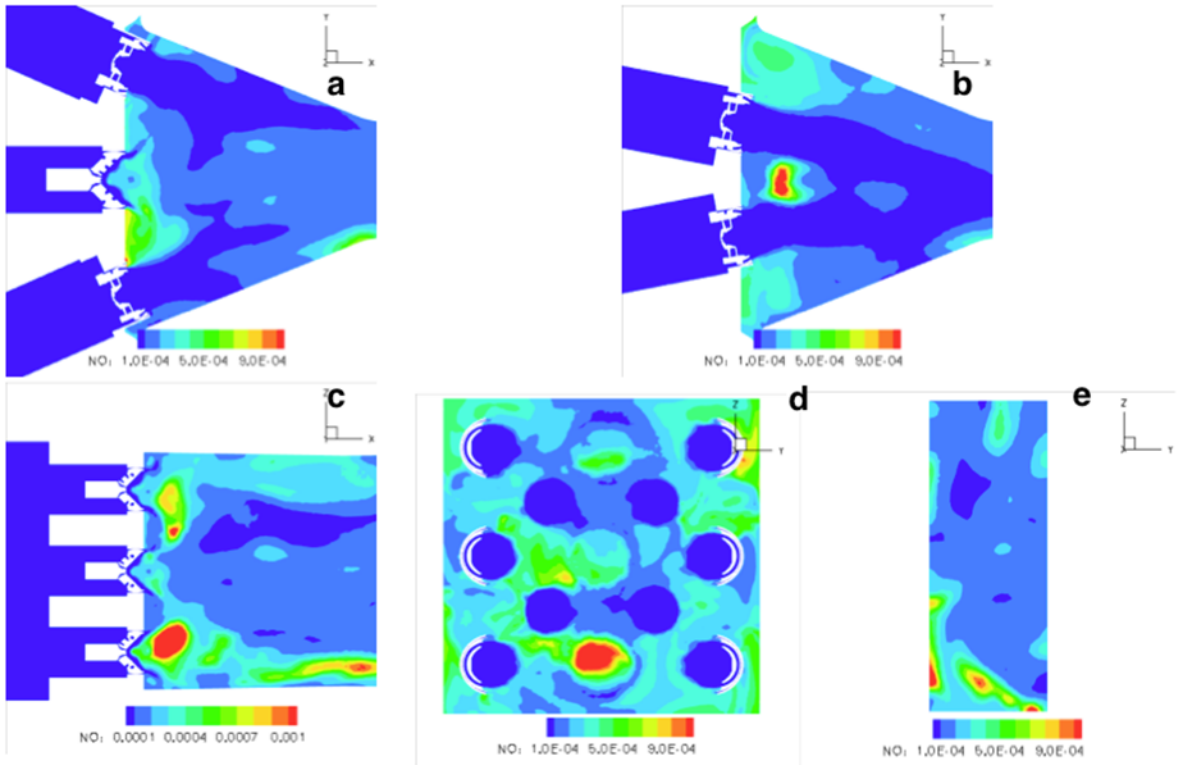

Figure 16 RDG192 – NOx mass-fraction contours (a) outers, pilot (b) intermediates (c) pilots (d) face (e) exit

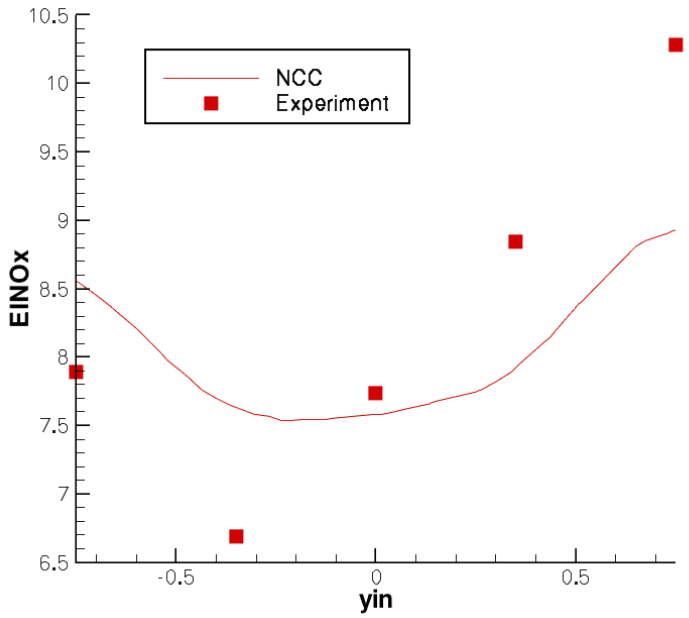

Figure 17 RDG 169 – Comparison of EINOx Traverse Data (NCC Computations vs. Experiment)

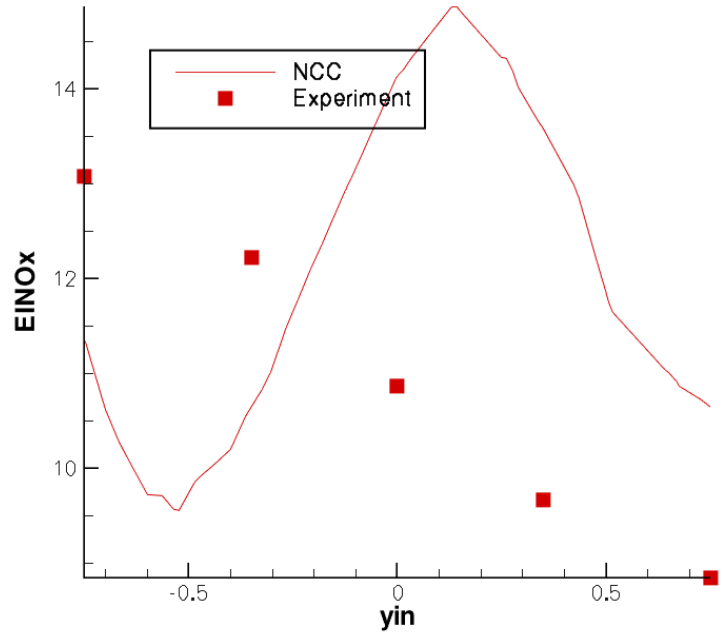

Figure 18 RDG 192 – Comparison of EINOx Traverse Data (NCC Computations vs. Experiment)

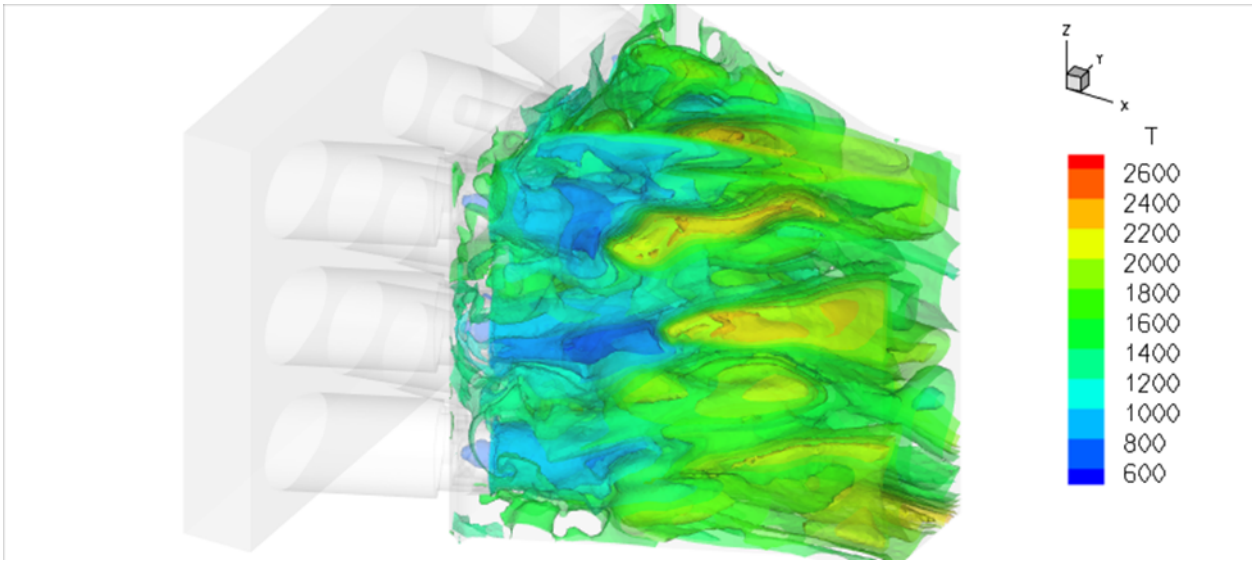

Figure 19 RDG 192 Case: Iso-surfaces of temperature (K) – Multiple-valued, showing mixing in combustor

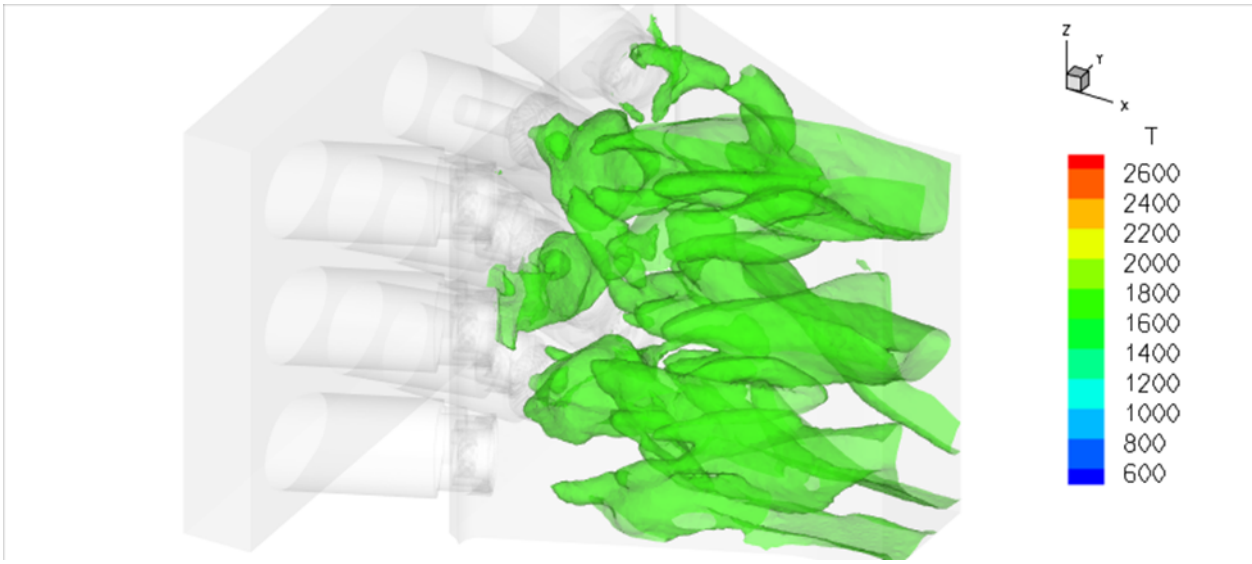

Figure 20 RDG 192 Case: Iso-surfaces of temperature (K) – Single-valued (1800K), showing swirl pattern of flames from injectors

References

[1] Prociw, A., Ryon, J., and Goeke, J., "Low NOx Combustion Concepts in Support of the NASA Environmentally Responsible Aircraft Program," GT2012-68426, Proceedings of the ASME Turbo Expo, June 2012.

[2] Tacina, R., Mao, C., and Wey, C., "Experimental Investigation of a Multiplex Fuel Injector Module with Discrete Jet Swirlers for Low Emission Combustors," AIAA 2004-0135, January 2004.

[3] Goeke, J., Pack, S., Zink, G., and Ryon, J., "Multi-Point Combustion System Final Report," NASA/CR-2014-218112.

[4] Bianco, J., "NASA Lewis Research Center's Combustor Test Facilities and Capabilities," AIAA-Paper 1995-2681, 1995.

[5] SAE ARP1256-2006, "Procedure for the Continuous Sampling and Measurement of Gaseous Emissions from Aircraft Turbine Engines."

[6] Liu, Nan-Suey, "Overview of the NCC," NASA CP-2001-211141, proceeding of the Tenth Thermal and Fluids Analysis Workshop, July 2001.

[7] Shih, T.-H., Povinelli, L.A., Liu, N.-S and Chen, K.-H., "Generalized Wall Function for Complex Turbulent Flows," NASA TM 2000-209936.

[8] Ajmani, K., Kundu, K. P. and Penko, P., "A Study on Detonation of Jet-A Using a Reduced Mechanism," 48th AIAA Aerospace Sciences Meeting, Orlando FL, AIAA Paper 2010-1515.

[9] Ajmani, K., Mongia, H.C. and Lee, P., "Evaluation of CFD Best Practices for Combustor Design: PART II – Reacting Flows," 51st AIAA Aerospace Sciences Meeting, Dallas TX, AIAA Paper 2013-1143.

[10] Raju, M. S., "LSPRAY-IV: A Lagrangian Spray Module," NASA CR-2012-217294.

Acknowledgements

NASA's Environmentally Responsible Aircraft (ERA) project office, and NASA's NAS Supercomputing Facility at NASA Ames Research Center supported the experimental and computational work described in this paper.